Available online at www.sciencedirect.com
SCIENCE DIRECT®
Journal of Nuclear Materials 326 (2004) 125–131
journal of nuclear materials
www.elsevier.com/locate/jnucmat

Effect of isothermal annealing on the corrosion behavior of Zr–xNb alloys

Hyun Gil Kim [a], Yong Hawn Jeong [a,*], To Hoon Kim [b]

[a] Zirconium Fuel Cladding Team, Korea Atomic Energy Research Institute, P.O. Box 105, Yuseong, Daejeon 305-600, South Korea
[b] Department of Materials Science and Engineering, Yonsei University, Sinchon-dong 134, Sedaemoon-ku, Seoul 120-749, South Korea

Received 22 July 2003; accepted 5 January 2004

Abstract

To study the effect of isothermal annealing on the corrosion behavior of Zr–xNb alloys, several systematic studies on corrosion and oxide characteristics were performed for the Zr–xNb alloys ($x = 0.1 \sim 2.0$ wt%). The samples were annealed at 570 °C for 0–1000 h after β-quenching. The corrosion resistance of the 0.1 and 0.2 wt% Nb alloys where Nb existed in the equilibrium soluble state in the matrix was excellent in the quenched and annealed conditions. For the high Nb-containing alloys, the corrosion rates were very sensitive to the annealing condition, and it took about 50 h at 570 °C to reach corrosion rates comparable to the low Nb wt% alloys. The corrosion resistance is correlated to the stabilization of the tetragonal ZrO_2 and columnar oxide structure when the Nb concentration in the matrix is reduced to the equilibrium soluble limit.

1. Introduction

Since Zr-based alloys have good irradiation stability and corrosion resistance in a reactor environment, they are being used as cladding and structural materials for nuclear fuel. However, recently, more advanced Zr-based alloys are required for severe operating conditions such as an increased burn-up and higher operation temperatures [1–4]. As the corrosion properties of the Nb-containing Zr alloys are known to depend on the microstructure, it is essential to investigate the effect of the Nb-content and the effect of annealing after beta quenching on the corrosion of Zr–xNb binary alloys, for developing advanced nuclear fuel cladding materials with improved corrosion resistance.

Investigation on the corrosion behavior of Zr–Nb binary alloys in relation to the microstructural changes have been reported [5–7]. In order to understand the separate effects of the microstructural changes in the α and β phases in the Zr–2.5% Nb pressure tube material Urbanic et al. have also investigated the corrosion behavior of Zr–Nb alloys, the Nb concentration varying from 0.02% to 1.35% Nb and of Zr–5Nb and of Zr–20Nb alloys [6]. They had annealed the specimens at 850 °C to simulate the metallurgical condition to be close to that of the pressure tube alloy. It is shown that (i) best corrosion resistance is associated with a Nb concentration close to the solid solubility in α-zirconium of 0.3–0.4 wt%, (ii) β-zirconium phase is associated with high corrosion and (iii) β-zirconium phase undergoes thermal decomposition, generating β-niobium precipitates and improving the corrosion resistance. In our study reported here, the annealing of the β-quenched specimens was performed close to the monotectoid temperature of 570 °C. We have characterized the second phase precipitated and the oxide films. Our findings confirm the conclusion reported by the previous researchers.

2. Experimental procedure

The alloys containing 0.1–2 wt% Nb were prepared by the manufacturing process shown in Fig. 1. After

* Corresponding author. Tel.: +82-42 868 2322; fax: +82-42 862 0432.
E-mail address: yhjeong@kaeri.re.kr (Y.H. Jeong).

0022-3115/$ - see front matter © 2004 Elsevier B.V. All rights reserved.
doi:10.1016/j.jnucmat.2004.01.015

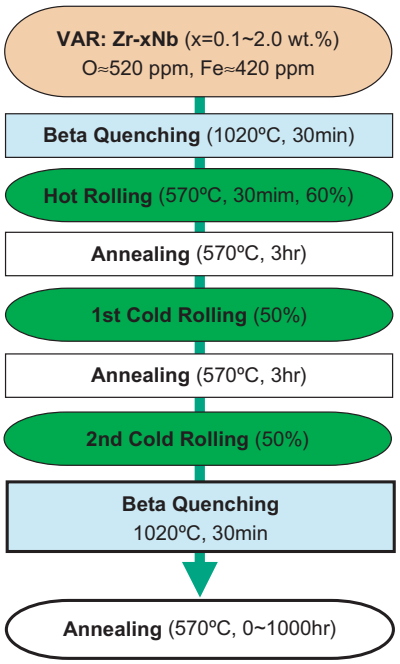

Fig. 1. Alloy composition and manufacturing process of Zr–*x*Nb alloys.

making the button-type ingots of 300 g in weight using vacuum arc re-melting, the ingots were processed as sheet-type specimens by applying hot rolling and cold rolling. The sheet samples were β-quenched at 1020 °C for 30 min to get homogeneous solution. The samples for β-quenching were inserted in evacuated quartz capsules to prevent oxidation during the β-heat treatment. The annealing of the β-quenched samples was carried out at 570 °C for 0 to 1000 h.

Generally, the monotectoid temperature of the Zr–Nb system is known to be 610 °C [8]. However, in our previous study [9], the monotectoid temperature of Zr–Nb binary alloys using sponge-type Zr was found to be 585 °C. Therefore, the annealing to get the β_{Nb} phase was performed at 570 °C in this study. The microstructure observation and the precipitates analysis of the samples were performed using a polarized optical microscope (OM) and a transmission electron microscope (TEM) equipped with EDS. The specimens for OM observation were etched with a solution of HF (10 vol.%), HNO_3 (45 vol.%), H_2O (45 vol.%). The specimens for TEM observation were chemically etched by twin jet-polisher with a solution of ethanol (90 vol.%) and perchloric acid (10 vol.%) under 15 V at −40 °C after they had been mechanically polished to a 70 μm thickness. The specimens for the corrosion test were pickled with the pickling solution of HF (5 vol.%), HNO_3 (45 vol.%), H_2O (50 vol.%) after they were mechanically polished with SiC polishing paper to minimize the surface effect on corrosion.

The corrosion tests of the specimens were carried out using a static autoclave at 360 °C in water and reducing conditions under about 18.9 MPa. The corrosion behaviors were evaluated by measuring the weight gains. The oxide films on the corroded specimens were analyzed using low angle X-ray diffraction (XRD) and TEM. The specimens for the oxide analysis were corroded for different test times from each other in order that they could have the same weight gain as much as possible. Low-angle XRD analyses were performed for all the oxide films applying the incident angle of 2° and the scan speed of 0.5°/min. The cross-section and plan-view of the oxide film were analyzed using TEM.

3. Results and discussion

3.1. Microstructures of Zr–Nb alloy with different annealing time

Fig. 2 shows the optical microstructures of the specimens with different Nb contents after different annealing times. In the case of the water-quenched specimens, the martensite microstructure got fine with the increased Nb-content. This result can be explained on the basis of the decrease in M_s temperature with increase in Nb content; the width of the martensite plates decreased due to the higher driving force in the high Nb alloy [10]. The quenched microstructures changed with the increase in annealing time. The microstructure of Zr–0.2Nb alloys showed a fully recrystallized structure when the sample was annealed at 570 °C for 5 h. It was also observed that the grains of Zr–0.8Nb alloy were partially grown to be coarse when they were annealed at 570 °C for 500 h, and then they were fully recrystallized after annealing for 1000 h. The microstructures of the Zr–1.5Nb alloy were too fine to clarify the recrystallized structure by an optical microscope even after annealing for 1000 h.

The grain size of the specimens could thus be controlled by the Nb content in the Zr–*x*Nb alloys. The grain of the low Nb alloys was easily grown with the increased annealing time while the grain growth of the high Nb alloys was difficult because the Nb-containing precipitates prevented grain growth. But it is hard to discuss such a thing with only optical observation. So, in order to find out the effect of the Nb content and precipitates on the microstructures of Zr–Nb alloys, TEM studies were performed for the quenched and annealed samples.

Fig. 3 shows the TEM microstructures of the quenched and annealed Zr–Nb alloys having 0.2, 0.8 and 1.5 wt% Nb when they were annealed at 570 °C for 5 and 50 h. Fine cell structures were observed in the TEM microstructures of Zr–0.2Nb. As the annealing time increased, the dislocations in the cell structures

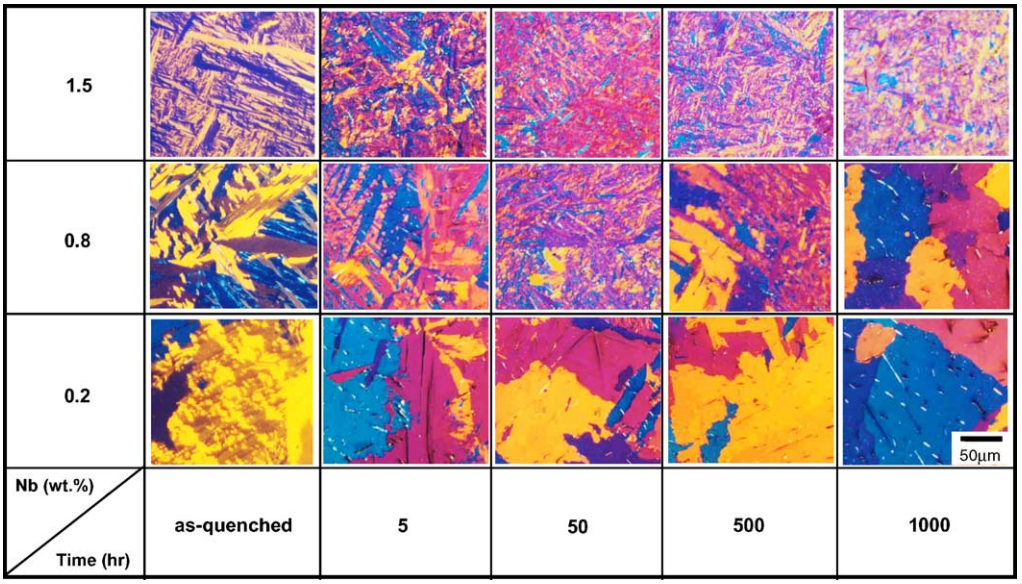

Fig. 2. Optical microstructures of Zr–*x*Nb alloys with annealing time for 0–1000 h at 570 °C.

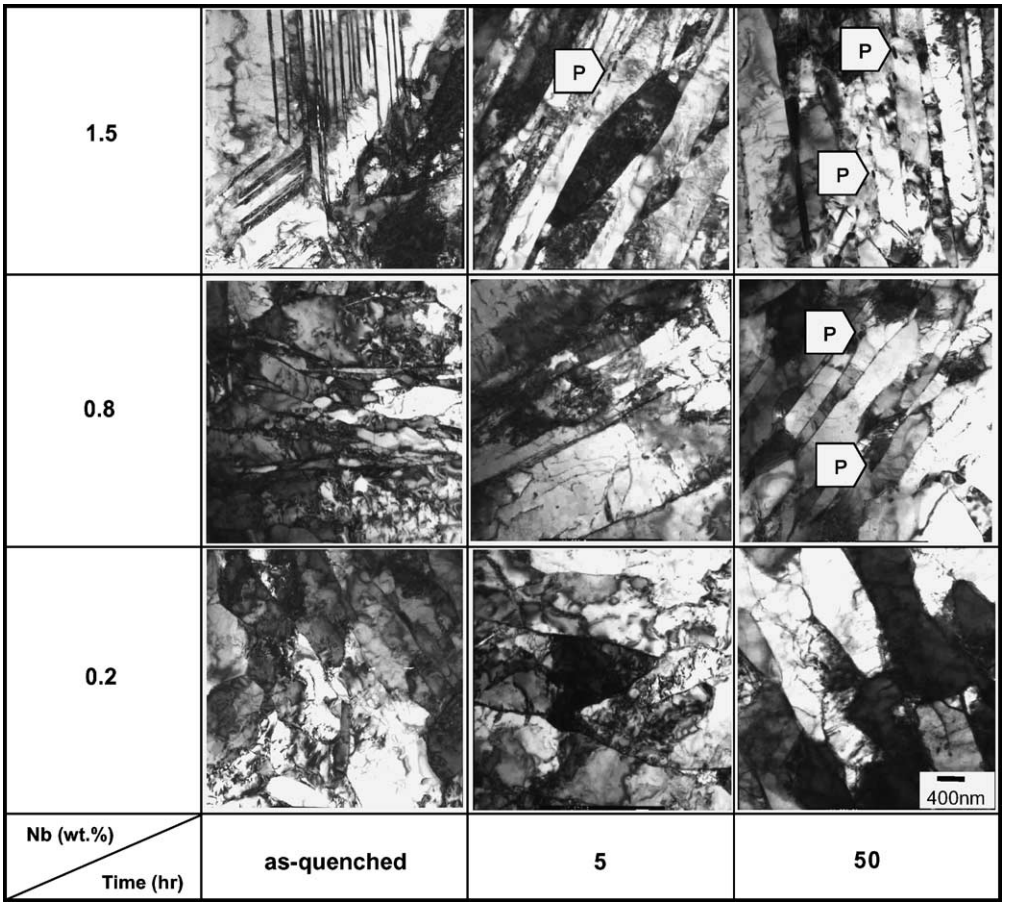

Fig. 3. TEM micrographs of Zr–*x*Nb alloys with annealing time for 0–50 h at 570 °C.

disappeared. In the case of the Zr–0.8Nb alloy, the internal dislocations which were introduced during quenching fully disappeared after 50 h annealing, and fine precipitates were observed at the plate boundaries. The Zr–1.5Nb alloys showed the substructures of internal twin and dislocation cells after quenching, and as the annealing time increased the substructures disappeared and many fine precipitates were formed at the plate boundaries. The characteristics of the precipitates are discussed later.

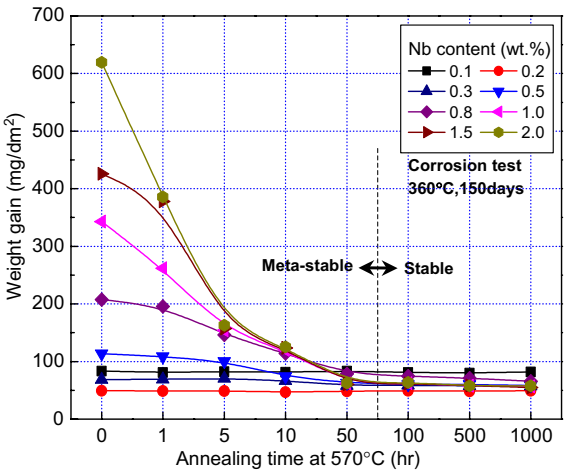

Fig. 4. Corrosion behavior of Zr–*x*Nb alloys as a function of annealing time at 570 °C.

3.2. Corrosion characteristics of Zr–Nb alloys

Fig. 4 shows the corrosion behavior of Zr–*x*Nb alloys tested at 360 °C for 150 days. For the quenched specimens, the weight gain increased with increasing Nb-content. And as the annealing time increased, the weight gain for Zr–Nb alloys containing more than 0.5 wt% Nb rapidly decreased and attained a constant value for 50–1000 h. But there were no changes in weight gains in the case of the Zr–Nb alloys containing Nb less than 0.3 wt% even after annealing up to 1000 h. Therefore, it might be said that in the case of the quenched Zr–Nb alloys having Nb content more than the solubility limit, it takes about 50 h of annealing at 570 °C to get the equilibrium condition of β_{Nb} precipitation and dissolved Nb in the α-matrix. This condition is associated with a good corrosion resistance [11,12].

It is believed from the effect of annealing on increasing the corrosion resistance that about 0.2 wt% would be the Nb solubility limit of Zr–Nb alloys made of commercial grade sponge Zr. This result from the corrosion behavior is consistent with the previous result for the phase boundary study using commercial grade sponge Zr [9].

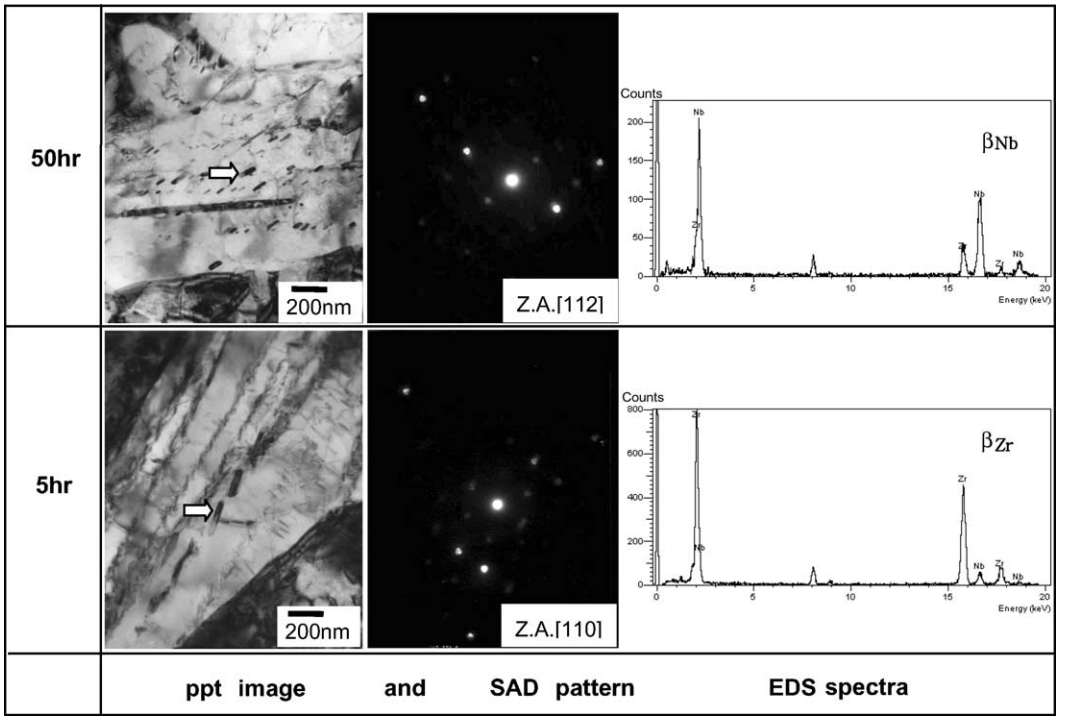

Fig. 5. Second phase particles in Zr–1.5Nb alloys with annealing time at 570 °C for 5 and 50 h after β-quenching.

3.3. Second phase particles of Zr–Nb alloys depending on annealing time

Fig. 5 shows the characteristics of the precipitates in Zr–1.5Nb alloy when it was isothermally heat-treated at 570 °C. Very fine precipitates were observed at twin or plate boundaries as well as at interior parts of the martensite. The SAD and EDS analysis on the precipitates showed that most of them after annealing for 5 h were β_{Zr} phases of BCC crystal structure containing ~14 wt% Nb. But after 50 h annealing, it was analyzed that most of the precipitates were β_{Nb} phases of BCC crystal structure containing ~80 wt% Nb. This means that the stable β_{Nb} phases could precipitate in the Zr–1.5Nb alloy after the annealing for 50 h at 570 °C. The β_{Zr} phase was slowly changed into the β_{Nb} phase with increase in annealing time.

Table 1 shows the summary of precipitates in the Zr–*x*Nb alloys with the annealing time. The Nb-containing precipitates were not formed in the Zr–0.2Nb alloy but a few Zr_3Fe precipitates having orthorhombic structure were found in this specimen because the sponge Zr used this study had Fe at 420 ppm as impurity. The $Zr(NbFe)_2$ precipitates of HCP structure were mainly observed in the Zr–0.8Nb alloy when it was annealed for 5 h and β_{Zr} phase was observed additionally in the specimen annealed for 50 h. In Zr–1.5Nb alloy, the β_{Zr} phase with a few $Zr(NbFe)_2$ were observed after the short-term annealing of 5 h, but the β_{Zr} phase was transformed to β_{Nb} phase after the annealing for 50 h.

Table 1
Summary of precipitates in Zr–*x*Nb alloys with annealing time at 570 °C

Annealing time (h)		Nb content (wt%)		
		0.2	0.8	1.5
5	Type	–	– $Zr(NbFe)_2$[a]	– $Zr(NbFe)_2$[b] β_{Zr}[a]
50	Type	Zr_3Fe[a] – –	– $Zr(NbFe)_2$[a] β_{Zr}[b]	– $Zr(NbFe)_2$[b] β_{Nb}[a]
500	Type	Zr_3Fe[a] – –	– $Zr(NbFe)_2$[a] β_{en}[b]	– $Zr(NbFe)_2$[b] β_{Nb}[a]

[a] Major particle.
[b] Minor particle.

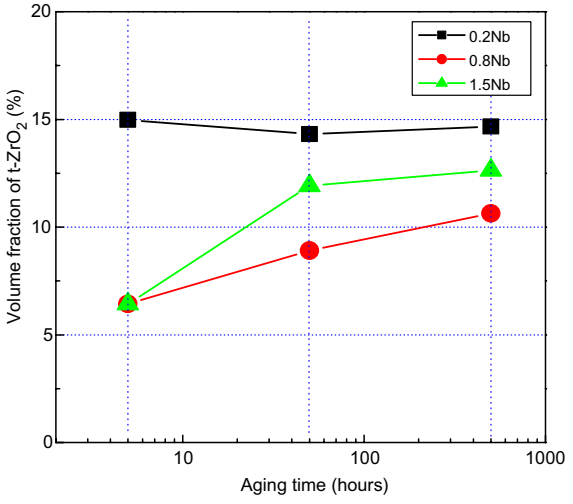

Fig. 6. Volume fraction of tetragonal ZrO_2 in zirconium oxide formed on Zr–*x*Nb alloys annealed at 570 °C for 50 h (equal oxide thickness at pre-transition).

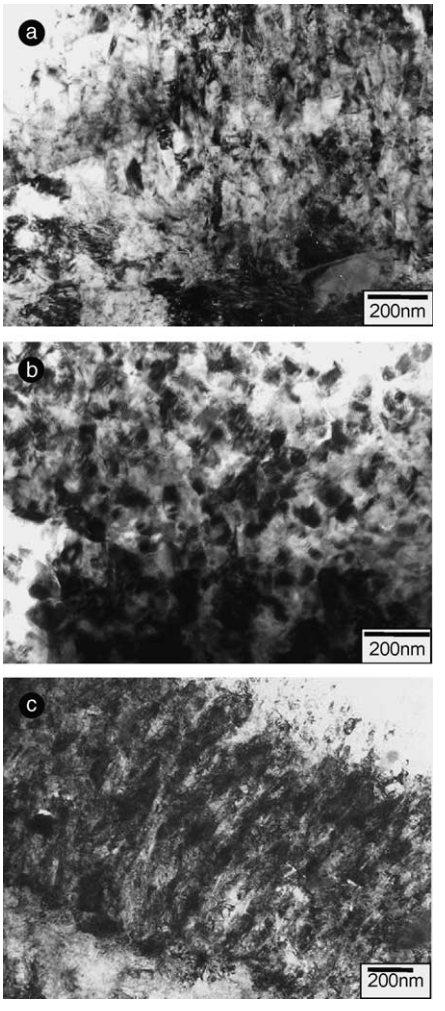

Fig. 7. Cross-sectional TEM micrographs of zirconium oxide at pre-transition. (a) 0.2Nb (as-quenched: equilibrium Nb). (b) 1.5Nb (as-quenched: supersaturated Nb). (c) 1.5Nb (570×500 h: β_{Nb} and equilibrium Nb).

3.4. Oxide characteristics

Fig. 6 reveals the volume fraction of tetragonal ZrO_2 in the oxides having an equal oxide thickness on the Zr–Nb alloys containing 0.2, 0.8, and 1.5 wt% Nb which had been annealed at 570 °C for 5, 50 and 500 h. For the Zr–0.2Nb alloy showing the good corrosion resistance, the volume fractions of tetragonal ZrO_2 were high regardless of the annealing time. But in the case of the Zr–0.8Nb and Zr–1.5Nb alloys, the volume fraction of tetragonal ZrO_2 gradually increased with the increased annealing time. The volume fractions of the tetragonal ZrO_2 in the Zr–1.5Nb alloy increased with the annealing time.

TEM analysis of the microstructure of oxide film can also be correlated to the corrosion resistance of the alloys [13–15]. Fig. 7 shows the TEM micrographs of Zr oxides on the Zr–0.2Nb and Zr–1.5Nb alloys. In the case of Zr–0.2Nb alloy, in which the Nb-concentration in the matrix was equal to the solubility limit, columnar oxide structure was developed in normal direction to the surface as shown in Fig. 7(a). But in the case of the Zr–1.5Nb, in which the Nb element existed at supersaturated state in the matrix, the oxide showed an equiaxed microstructure. When Zr–1.5Nb alloy was annealed at 570 °C for 500 h, columnar oxide developed.

In order to characterize the oxide at the metal–oxide interface, TEM samples of oxide were prepared by the dissolution of metal part and then by ion milling in the perpendicular direction to the oxide surface. Fig. 8 shows the HR-TEM image in a plane-view of oxide film formed in the quenched Zr–0.2Nb alloy that showed a good corrosion resistance. As shown in Fig. 8(a), the oxide microstructures were observed to be equiaxed type and the grain size was about 15–70 nm. It is not clear from the plane-view microstructure whether this type oxide is columnar structure or not. However, the oxide formed on the Zr–0.2Nb alloy has already been identified as columnar, Fig. 7(a). Fig. 8(b) shows the lattice image of oxide observed by HR-TEM. The oxide crystal structure consisted of the mixed structures of tetragonal ZrO_2 and monoclinic ZrO_2. The formation of tetragonal ZrO_2 at local areas could be related to the good corrosion resistance of the Zr–0.2Nb alloy.

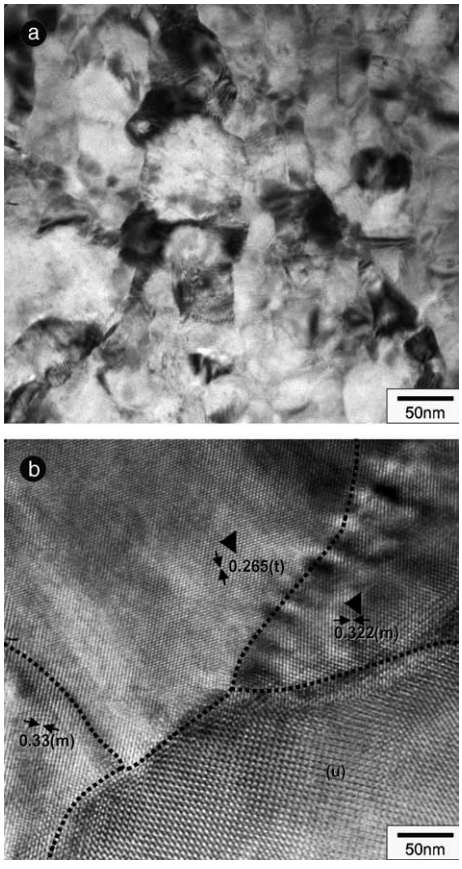

Fig. 8. Plane-view TEM micrographs of zirconium oxide in the quenched Zr–0.2Nb alloy. (a) Plane-view image, (b) lattice image.

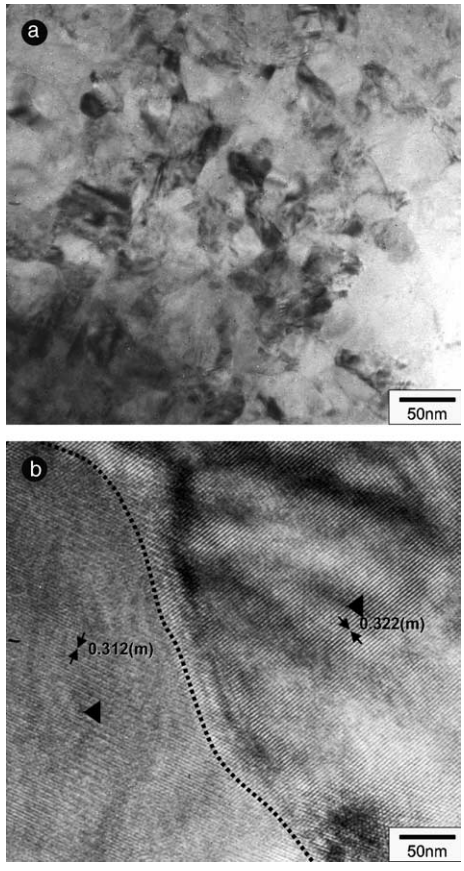

Fig. 9. Plane-view TEM micrographs of zirconium oxide in the quenched Zr–1.5Nb alloy. (a) Plane-view image, (b) lattice image.

Fig. 9 shows the oxide microstructure formed on the quenched Zr–1.5Nb alloy matrix which showed a poor corrosion resistance. As shown in Fig. 9(a), the oxide microstructure was also observed to be equiaxed type and the grain size was about 10–55 nm, which was smaller than that in Zr–0.2Nb alloy. Fig. 9(b) shows the HR-TEM micrographs of the oxide at metal–oxide interface. The oxide was identified as monoclinic ZrO_2 without tetragonal ZrO_2. It is suggested that an absence of tetragonal ZrO_2 and small grain size could be related to the poor corrosion resistance of the alloys.

4. Conclusion

The corrosion behavior of Nb-containing Zr alloys was studied for the Zr–xNb binary alloys with variations of Nb-content and annealing time at 570 °C. In the quenched specimens without annealing, the weight gain increased with the increased Nb-content. As the annealing time increased, the weight gains of Zr–Nb alloys containing Nb more than 0.5 wt% rapidly decreased, and remained nearly steady after the annealing for 50 h. There was no big change in the weight gain in the case of the Zr–Nb containing Nb less than 0.3 wt%. It was found that the corrosion resistance of the Zr–Nb alloys was excellent when the Nb concentration in the matrix was equal to the soluble limit. The improved corrosion resistance of Zr–Nb alloys is related to the stabilization of tetragonal ZrO_2 and columnar oxide structure.

Acknowledgements

This project has been carried out under the Nuclear Fuel R&D program by MOST in KAERI.

References

[1] G.P. Sabol, G.R. Kilp, M.G. Balfour, E. Roberts, ASTM STP 1023 (1989) 227.
[2] A.V. Nikulina, Y.K. Bibilashvili, P.P. Markelov, M.M. Peregu, V.A. Koterekhov, A.F. Lositsky, N.Y. Kuzmenko, Y.P. Shevnin, V.K. Shamardin, G.P. Kobylyansky, A.E. Novoselov, ASTM STP 1295 (1996) 785.
[3] J.P. Mardon, G. Garner, P. Beslu, D. Charquet, J. Senevat, in: Proceedings of the 1997 International Topical Meeting on LWR Fuel Performance, Portland, Oregon, 2–6 March 1997, p. 405.
[4] S. Suzuki, K. Murakami, T. Takahashi, in: Proceedings of the 1994 International Topical Meeting on LWR Fuel Performance, West Palm Beach, Florida, 17–21 April 1994, p. 352.
[5] V.F. Urbanic, P.K. Chan, D. Khatamian, O.T. Woo, ASTM STP 1245 (1994) 116.
[6] V.F. Urbanic, M. Griffiths, ASTM STP 1354 (2000) 641.
[7] G.P. Sabol, R.J. Comstock, U.P. Nayak, ASTM STP 1354 (2000) 525.
[8] C.E. Lundin, R.H. Cox, USAEC Report GEAP 4089, 1962, p. 9.
[9] J.Y. Park, Y.S. Kim, H.G. Kim, Y.H. Jeong, in: Proceedings of ENS Top fuel 2003, Würzburg, Germany, 16–19 March 2003.
[10] D. Stewart, B.A. Hatt, J.A. Roberts, Br. J. Appl. Phys. 16 (1965) 1081.
[11] D.J. Kim, H.G. Kim, S.I. Hong, Y.H. Jeong, J. Kor. Inst. Met. Mater. 40 (2002) 692.
[12] Y.H. Jeong, K.O. Lee, H.G. Kim, J. Nucl. Mater. 302 (2002) 9.
[13] F. Garzarolli, H. Seidel, R. Tricot, J.P. Gros, ASTM STP 1132 (1991) 395.
[14] H. Anada, K. Takeda, ASTM STP 1295 (1996) 35.
[15] Y.H. Jeong, J.H. Baek, S.J. Kim, H.G. Kim, H. Ruhmann, J. Nucl. Mater. 270 (1999) 322.